context, particular attention must be paid to the technical parameters associated with optimal gallium scanning. High doses (185–296 MBq) will allow increased diagnostic performance, particularly on delayed images because the tumor-to-background ratio increases with time. Acceptable counting rates can be achieved even up to 4–5 days after radionuclide injection.

CONCLUSION

Gallium-67 scanning seems to be the best modality available for evaluating treatment response and predicting outcome in patients with diffuse small and large cell lymphoma. Persistent ^{67}Ga uptake after four cycles of polychemotherapy may justify a change of therapy.

REFERENCES

1. Shipp MA, Harrington DP, Anderson JR, et al. A predictive model for aggressive non-Hodgkin's lymphoma. *N Engl J Med* 1993;329:987–994.
2. DeVita VT, Hubbard SM, Young RC, et al. The role of chemotherapy in diffuse aggressive lymphomas. *Semin Hematol* 1988;25:2–10.
3. Jochelson M, Mauch P, Bilikian J, Rosenthal D, Canellos G. The significance of the residual mediastinal mass in treated Hodgkin's disease. *J Clin Oncol* 1985;3:637–640.
4. Israel O, Front D, Ebelbaum R, et al. Residual mass and negative gallium scintigraphy in treated lymphoma. *J Nucl Med* 1990;31:365–368.
5. Wylie BR, Southee AE, Joshua DE. Gallium scanning in the management of mediastinal Hodgkin's disease. *Eur J Haematol* 1989;42:344–347.
6. Lewis E, Bernardino ME, Salvator PG, Cabanillas FF, Barnes PA, Thomas JL. Post-therapy CT-detected mass in lymphoma patients: is it viable tissue? *J Comput Assist Tomogr* 1982;6:792–795.
7. Chen JL, Osborne BM, Butler JJ. Residual fibrous masses in treated Hodgkin's disease. *Cancer* 1987;60:407–413.
8. Radford JA, Cowan RA, Flanagan M, et al. The significance of residual mediastinal abnormality on the chest radiograph following treatment for Hodgkin's disease. *J Clin Oncol* 1988;6:940–946.
9. Front D, Ben-Haim S, Israel O, et al. Lymphoma: predictive value of Ga-67 scintigraphy after treatment. *Radiology* 1992;182:359–363.
10. Karimjee S, Brada M, Husband J, McCready VR. A comparison of gallium-67 single photon emission computed tomography and computed tomography in mediastinal Hodgkin's disease. *Eur J Cancer* 1992;28A:1856–1857.
11. Tesoro-Tess JD, Balzarini L, Ceglia E, et al. Magnetic resonance imaging in the initial staging of Hodgkin's disease and non-Hodgkin's lymphoma. *Eur J Radiology* 1991;12:81–90.
12. Hill M, Cunningham D, MacVicar D, et al. Role of magnetic resonance imaging in predicting relapses in residual masses after treatment of lymphoma. *J Clin Oncol* 1993;11:2273–2278.
13. Gasparini M, Balzarini L, Castellani MR, et al. Current role of gallium scan and magnetic resonance imaging in the management of mediastinal Hodgkin lymphoma. *Cancer* 1993;72:577–582.
14. Nyman RS, Rehn SM, Glimelius BLG, et al. Residual mediastinal masses in Hodgkin's disease: prediction of size with MR imaging. *Radiology* 1989;170:435–440.
15. Frija J, Bris C, Yarner C, et al. MRI with gadolinium of post therapeutic residual masses in lymphoma [Abstract]. *Eur J Radiol* 1991;1(suppl):17.
16. Okada J, Yoshikawa K, Imazeky K, et al. The use of FDG PET in the detection and management of malignant lymphoma: correlation of uptake with prognosis. *J Nucl Med* 1991;32:686–691.
17. Leskinen-Kallio S, Ruotsalainen U, Nagren K, Teras M, Joensum H. Uptake of carbon-11-methionine and fluorodeoxyglucose in non-Hodgkin's lymphoma: a PET study. *J Nucl Med* 1991;32:1211–1218.
18. Kubota R, Yamada S, Kubota K, Ishiwata K, Ido T. Microautoradiographic study of F-18-FDG: high accumulation in granulation tissues and phagocytes in mouse tumor in vivo [Abstract]. *J Nucl Med* 1992;33:840.
19. Wahl RL, Clavo A, Brown RS, Roessner J. 2-Fluoro-2-deoxy-D-glucose (FDG) uptake into human cancer cell lines is increased by hypoxia [Abstract]. *J Nucl Med* 1992;33:841.
20. Iosilevski G, Front D, Bettman L, et al. Uptake of gallium-67 citrate and [2-H^3]deoxyglucose in the tumor model, following chemotherapy and radiotherapy. *J Nucl Med* 1985;26:278–282.
21. Straus DJ. Modern approaches for Hodgkin's disease. *Curr Opin Oncol* 1993;5:785–790.
22. von Gunten CF, Gordon LI. Treatment of advanced, aggressive non-Hodgkin's lymphoma. *Curr Opin Oncol* 1993;5:791–796.
23. Peylan-Ramu N, Haddy TB, Jones E, et al. High frequency of benign mediastinal uptake of gallium-67 after completion of chemotherapy in children with high-grade non-Hodgkin's lymphoma. *J Clin Oncol* 1989;7:1800–1806.
24. Canellos GP. Residual mass in lymphoma may not be residual disease. *J Clin Oncol* 1988;6:931–933.
25. Stewart FM, Williamson BR, Innes DJ, et al. Residual tumor masses following treatment for advanced histiocytic lymphoma. Diagnostic and therapeutic implications. *Cancer* 1985;55:620–623.
26. Armitage JO, Weisenburger DD, Hutchins M, et al. Chemotherapy for diffuse large cell lymphoma: rapidly responding patients have more durable remissions. *J Clin Oncol* 1986;4:160–164.
27. Kaplan WD, Jochelson MS, Herman TS, et al. Gallium-67 imaging: a predictor of residual tumor viability and clinical outcome in patients with diffuse large-cell lymphoma. *J Clin Oncol* 1990;8:1966–1970.
28. Newman JS, Francis IR, Kaminski MS, et al. Imaging of lymphoma with PET with 2-[F-18]-fluoro-deoxy-d-glucose: correlation with CT. *Radiology* 1994;190:111–116.
29. Heokstra OS, Ossenkoppele GJ, Golding R, et al. Early treatment response in malignant lymphoma, as determined by planar fluorine-18-fluorodeoxyglucose scintigraphy. *J Nucl Med* 1993;34:1706–1710.

Impact of Scatter Correction in Planar Scintimammography: A Phantom Study

Irène Buvat, Marie Carmen De Sousa, Mireille Di Paola, Marcel Ricard, Jean Lumbroso and Bernard Aubert

Unité 66, INSERM, CHU Pitié-Salpêtrière, Paris, and Unité de Physique en Imagerie, Institut Gustave-Roussy, Villejuif, France

This study examines how scatter correction might affect lesion detection and quantitation of tumor-to-normal breast tissue activity ratio in planar scintimammography. **Methods:** Forty-one phantom acquisitions were performed to mimic a wide variety of scintimammographic imaging conditions in which lesions would be close to the chest wall. For each acquisition, the images corresponding to a 10% energy window (I10) and two scatter correction methods [the Jaszczak (JA) method and a factor analysis (FA)-based method] were obtained in addition to the conventional 20% image (I20). A total of 368 images in which detection of the "tumor" was judged borderline were selected, and 10 independent observers were asked to detect lesions in these images. Receiver operating curve analyses were performed to assess detection performance. Tumor-to-normal tissue activity ratios were calculated for quantitative analysis. **Results:** Detection performance significantly improved for the I10, JA and FA images compared to the I20 images, with an increase in sensitivity up to 8% for FA images. Sensitivity was especially increased for small lesions (13- and 16-mm^3 spheres) and true heart-to-normal tissue activity ratios of >12. Scatter correction also increased the certainty with which the readers gave their judgment. The tumor-to-normal tissue activity ratio was ~8% larger on JA or FA images and 1% larger on the I10 images compared to the I20 images. For a given image, the variability with which this ratio was estimated was reduced by ~4% on JA and FA images. **Conclusion:** Based on these phantom results, scatter correction might be used with benefit in scintimammography.

Key Words: scatter correction; scintimammography; receiver operating curve analysis; quantitation

J Nucl Med 1998; 39:1590–1596

Received Aug. 5, 1997; revision accepted Nov. 24, 1997.

For correspondence or reprints contact: Irène Buvat, PhD, Unité 66 INSERM/CNRS, CHU Pitié-Salpêtrière, 91 Boulevard de l'Hôpital, 75634 Paris Cedex 13, France.

Breast cancer is one of the leading causes of cancer-related death in women in developed countries. Until now, physical examination and mammography were the primary tools in the detection of breast cancer. However, the poor specificity of mammography yields a high rate of unnecessary surgical procedures. Moreover, mammography of dense or operated breast causes additional problems. The problem of low specificity was one of the reasons why nuclear medicine appeared in the field of breast cancer diagnosis. Since 1994, ^{99m}Tc-sestamibi has been used for breast imaging, and many authors have reported favorable results (*1–6*). Overall sensitivity is between 80% and 100% depending on the patient population and selection bias, whereas specificity varies from 70% to 95%. However, it has been shown that the size and the location of the lesion in the breast are of crucial importance. Several studies have demonstrated an important decrease in sensitivity for small and nonpalpable lesions (typically <1.2 cm in diameter) (*1,2,4,5,7*). Although SPECT might improve these results (*8*), the absence of landmarks makes localization of abnormalities difficult, and SPECT has not yet been proven to present definite advantage over planar scintimammography. A reason why small, deep or poorly contrasted lesions are difficult to detect is the limited performance of the gamma cameras. A major phenomenon responsible for the poor spatial resolution and contrast in planar scintigraphy is scatter. Scatter is especially a concern for deep lesions and also for lesions that are close to the chest wall because of the high heart activity from which many photons originate, creating a halo of scatter in the surrounding regions. Many scatter correction schemes have been described in the literature to improve both image quality and image quantitation (*9*). However, few authors have reported the impact of scatter correction in clinical configurations (*10–16*), and none of these studies were dedicated to scintimammography. The purpose of this work was to investigate how scatter correction might affect planar scintimammography in two respects:

1. Performance in lesion detection.
2. Quantitation of the tumor-to-nontumor activity ratio.

Phantom studies were conducted to mimic scintimammographic imaging conditions, while controlling for all phantom parameters. Receiver operating curve (ROC) analyses and quantitative measurements were performed to assess the effects of three different scatter correction methods compared to the 20% images conventionally used in clinical routine.

MATERIALS AND METHODS

Phantom Experiments

The phantom used for all experiments (Fig. 1A) consisted of a large Perspex cylinder B, simulating normal breast tissue activity (background), in which a smaller Perspex cylinder H, simulating heart activity, was fixed. Three hollow spheres (13, 16 and 28 mm in diameter) could be attached to the cylinder H at 90° each, at two different depths (5 and 10 cm from the bottom of the phantom). All compartments (B, H and the spheres S) were filled with different concentrations of ^{99m}Tc. Planar views of the phantom (Fig. 1B) were acquired using a GE Starcam gamma camera (GE Medical Systems, Milwaukee, WI), equipped with a low-energy, high-resolution collimator, in contact with the bottom of the phantom (Fig. 1A). Forty-one acquisitions with three hot spheres were performed by combining different phantom parameters (sphere depth equal to 5 or 10 cm, sphere-to-background (S/B) activity ratios varying from 2 to 23, sphere-to-heart (S/H) activity ratios set to 1, 0.526 or 0.344). Each acquisition was performed in list mode recording energy information, and 5 million counts were acquired in the 50–182 keV range, corresponding to at least 2 million events in the conventional 20% ^{99m}Tc energy window (126–154 keV). For each acquisition, the list mode was processed to consider three different counting statistics: 0.5, 1 and 2 million counts in the 20% energy window.

Scatter Correction Methods

For each acquisition and each counting statistic, four images (128 × 128; pixel size = 1.95 mm) were created from the list mode:

1. I20, corresponding to the conventional 20% image (126–154 keV).
2. I10, corresponding to a 10% wide energy window centered on the photopeak (133–147 keV).
3. JA, obtained from the Jaszczak method (*17*): the 92–125 keV Compton image was created, multiplied by the scaling factor k = 0.5 and subtracted from the 20% window image, to yield the scatter-corrected image JA.
4. FA, obtained from a factor analysis-based scatter correction (*18,19*). For each acquisition, a series of 33 spectral images was calculated, from 50–182 keV with a 4-keV sampling. The series was processed using factor analysis for spectral image sequences. This method assumes that the energy spectrum of the photons detected in each pixel is the weighted sum of a photopeak and two scatter spectra. These "basis" spectra are supposed to be common to all pixels and to belong to a "study" space resulting from the orthogonal analysis of the set of pixel spectra. In this study space, the photopeak was estimated using target apex-seeking (*18*), assuming it should be zero from 50 to 122 keV. No information regarding its shape in the 122–182 keV range was required. The two Compton spectra were estimated in an iterative way using nonnegativity constraints. The images associated with the basis spectra were calculated using a multidimensional projection of the original pixel spectra onto the three basis spectra. The image associated with the photopeak gave the scatter-corrected image FA.

This yielded a total of 492 images (41 acquisitions × 3 counting statistics × 4 types of images).

Visual Analysis

To obtain a database for visual analysis, each image was divided into four quadrants as shown in Figure 2, yielding four 64 × 64 subimages. Each subimage contained one or no sphere. An experienced observer examined all 20% subimages, ignoring whether they contained a sphere, and subjectively selected all 20% subimages for which the decision to whether there was a sphere was judged difficult. Only these borderline subimages were included in the image base. The corresponding scatter-corrected subimages I10, JA and FA were retrieved and added to the image base.

The resulting image base was read by 10 independent observers on a computer screen. Each observer first underwent a training session, using images different from those included in the image base, to become familiar with the detection task; the images were shown to the observers, and the correct answer (sphere present or absent) was given for each image. After training, the image base was presented independently to each observer, who scored the images using the following scale: 1 = sphere definitely present; 2 = sphere probably present; 3 = equivocal; 4 = sphere probably absent; and 5 = sphere definitely absent. All images were displayed using a rainbow-type color scale, and the observers were free to adjust the contrast of the display to help them interpret the images. No information was given to the observers as to the distribution of images with and without a sphere in the image base.

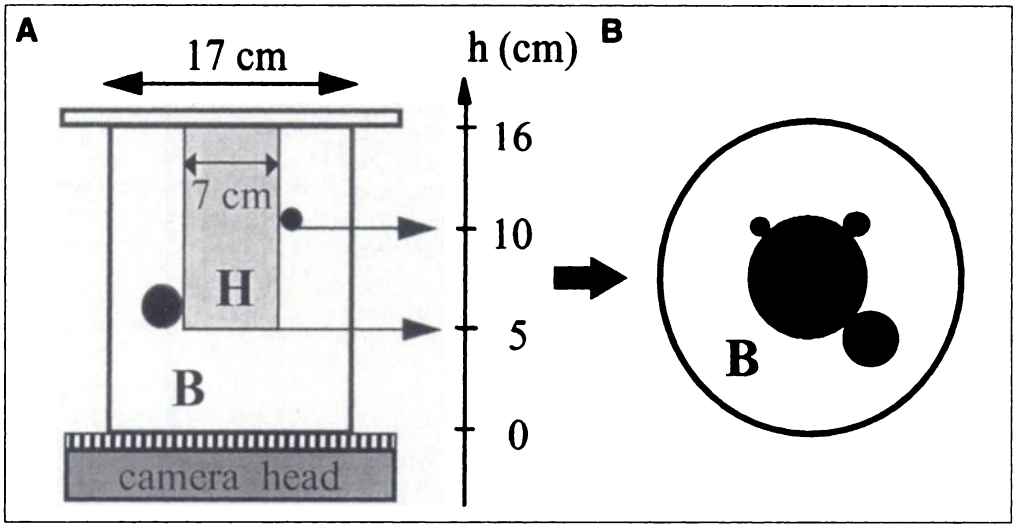

FIGURE 1. (A) Phantom used for the experiments. Cylinder H simulated heart activity, cylinder B simulated normal breast tissue, while the spheres represented the tumors. (B) Corresponding planar view of the phantom.

Quantitative Analysis

The tumor-to-normal breast tissue activity ratio is an index used in scintimammography image analysis in an attempt to characterize the malignancy of the tumor (*3*). To study the effect of scatter correction on the tumor-to-nontumor activity ratios, all 123 20% images were examined by an experienced observer who selected only those images where the largest sphere (28 mm in diameter) could be seen without ambiguity. This resulted in a subset of 45 20% images. Nine square regions of interest (ROIs) (4 × 4 pixels in size) were manually drawn by the observer on each of these 45 images, one over the largest sphere and eight at various locations over the background. The total number of counts in each of these regions was calculated, and eight values of the S/B activity ratio were deduced as well as the mean r and s.d. (σ) of these eight values. For a given image, the variability of the S/B activity ratio depending on the location of the background ROI was characterized by calculating $100 \times \sigma/r$. The same ROIs were reported on the I10, JA and FA scatter-corrected images, and the same calculations were performed.

RESULTS

Visual Analysis

Among all I20 subimages, 92 I20 images were judged to yield a nontrivial decision as to whether they contained a sphere. As a result, the image base presented to the observers contained 368 images (92 × 4 types of images): 72 images with a 13-mm^3 sphere, 84 with a 16-mm^3 sphere, 56 with a 28-mm^3 sphere and 156 without any sphere. For 68 images, the sphere was 5 cm deep, whereas it was 10 cm deep for 144 images. Detailed characteristics of the images are given in Table 1.

For each observer and each type of image, the ROC curve characterizing the detection performance was calculated as well as the area under the curve (Table 2). For all 10 observers, the poorest performance for the detection task, as quantified by the area under the ROC curve, was observed for the I20 images. For 8 of 10 observers, the best performance was observed using the FA images. Paired Wilcoxon tests (PWTs) were used to test whether the differences between ROC areas were significant. I10, JA and FA all yielded significantly better detection performance than I20 images ($p < 0.01$). FA images gave results significantly better than any other type of images ($p < 0.05$). There was no significant difference between JA and I10 images.

Sensitivity and specificity values were calculated for each observer and each type of image, for a decision threshold set to 3. The average sensitivity values over all observers were 74 ± 15%, 79 ± 14%, 78 ± 12% and 82 ± 13% for the I20, I10, JA and FA images, respectively. The corresponding specificity values were 83% ± 15%, 84% ± 12%, 86% ± 8% and 89% ± 8% for the I20, I10, JA and FA images. The sensitivity was significantly higher for the I10, JA and FA images compared to the I20 images (PWT at $p < 0.05$), but no other differences could be shown to be significant. The specificity was only significantly higher for FA compared to I10 images ($p < 0.05$).

Table 3 shows the median sensitivity values over all observers, for a decision threshold set to 3, as a function of sphere size and depth. The larger the sphere, the higher the sensitivity. The 13-mm^3 spheres were generally not detected at a 10-cm depth (very low sensitivity values) but became detectable at a 5-cm depth. JA and FA methods significantly improved detection sensitivity at a 10-cm depth compared to I20 images (PWT at $p < 0.05$), but the sensitivity remained poor. For the 16-mm^3 spheres, the sensitivity was not significantly different at a 5- or 10-cm depth, but note that the average S/B activity ratio was more than 3 times higher in the 10-cm-deep spheres than in the 5-cm-deep spheres (Table 1). At a 10-cm depth, the sensitivity was significantly higher with I10 and FA than with I20, and FA gave a significantly higher sensitivity than I10 or JA. For the 28-mm spheres, sensitivity was not significantly different for the two depths, and all types of images gave nonsignificantly different sensitivity values.

Observing the effect of the heart-to-background (H/B) activity ratio on sphere detection sensitivity (Table 4), the sensitivity was significantly higher when H/B was less than 12 (corresponding to an observed H/B ratio of less than ~6) compared to H/B greater than 12 for all methods (PWT at $p < 0.05$). For high heart activity (H/B > 12), I10, JA and FA presented a

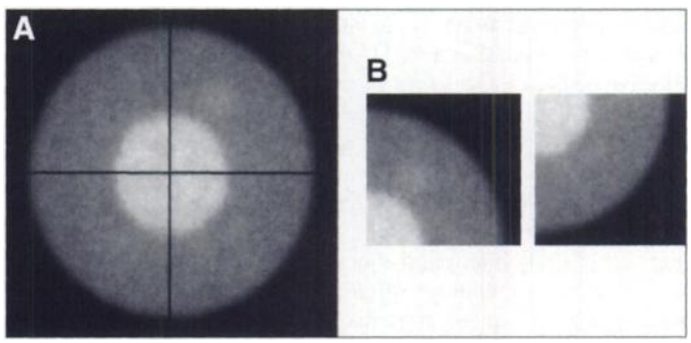

FIGURE 2. (A) To obtain the image base used for visual analysis, each image was divided into four quadrants, yielding four subimages. (B) Examples of corresponding subimages.

TABLE 1
Contents of Image Base Used for Visual Analysis

	13-mm sphere		16-mm sphere		28-mm sphere	
	5-cm sphere	10-cm depth	5-cm depth	10-cm depth	5-cm depth	10-cm depth
No. of images	28	44	28	56	12	44
Average true value of S/B activity ratio	4.8 ± 2.0	13.4 ± 5.7	3.7 ± 0.9	12.3 ± 5.4	2.1 ± 0.2	3.6 ± 0.8
S/H activity ratio	1 0.52 0.344		1 0.526 0.344		1 0.526 0.344	
No. of images	12 32 28		16 32 36		20 12 24	

S/B = sphere-to-background; S/H = sphere-to-heart.

sensitivity that was significantly higher than that observed for I20. For low heart activity, I10, JA or FA scatter corrections did not significantly increase the sphere detection sensitivity.

The degree of decision certainty was studied by counting the number of definite and correct answers (accurate scores of 1 or 5), the number of definite but incorrect answers (inaccurate scores of 1 or 5) and the number of equivocal answers (scores of 3). Table 5 gives a summary of the distribution of the scores, obtained by summing up all scores given by all 10 observers. For all but one observer, the lowest number of definite and accurate answers was recorded when the I20 images were interpreted. For 8 of 10 observers, the highest number of definite and accurate answers was observed using the FA images. The number of definite and accurate answers was significantly higher when I10, JA or FA images were used compared to I20 images (PWT at $p < 0.01$). FA images yielded a significantly higher number of accurate and definite judgments compared to any other images (PWT at $p < 0.05$).

TABLE 2
Areas Under the Receiver Operating Characteristic Curves for Different Observers and Types of Images

Observer	I20	I10	JA	FA
1	0.84*	0.90	0.87	0.93†
2	0.84*	0.89	0.87	0.97†
3	0.92*	0.94	0.93	0.96†
4	0.85*	0.86	0.92†	0.92†
5	0.89*	0.95†	0.93	0.92
6	0.88*	0.91	0.91	0.93†
7	0.68*	0.69	0.72	0.80†
8	0.87*	0.93	0.90	0.97†
9	0.84*	0.89	0.86	0.91†
10	0.86*	0.88	0.93†	0.89

*Lowest areas for a given observer.
†Largest areas for a given observer.
FA = factor analysis; I10 = 10% energy window; I20 = 20% energy window; JA = Jaszczak method.

The numbers of definite and inaccurate judgments were significant lower for I10, JA or FA images (PWT at $p < 0.01$) compared to I20 images, but no significant differences were found among I10, JA and FA images.

Finally, analysis of the numbers of equivocal answers using PWTs did not show any significant difference between the different types of images. However, there was a definite trend toward less equivocal answers when scatter-corrected images were used compared to the I20 images (Table 5).

Quantitative Analysis

Sphere-to-Background Activity Ratio. The mean S/B activity ratio r varied from 1.09 to 3.04 in the I20 images, from 1.07 to 3.31 in the I10 images, from 1.05 to 5.14 in the JA images and from 1.04 to 4.46 in the FA images. The mean values of $100 \times (r_{corr} - r_{I20})/r_{I20}$ ($r_{corr} = r_{I10}$, r_{JA} and r_{FA}, respectively), representing the average change in r caused by scatter correction compared to the I20 images, are given in Table 6 together with the results of PWTs. The r values were significantly higher when calculated from I10, JA or FA images compared to the I20 images. For the 5-cm-deep spheres, the true S/B activity ratio was underestimated by 58 ± 13% on the I20 images. Although the underestimation was systematically smaller for the scatter-corrected images, it was of the same order (57 ± 13%, 56 ± 11% and 56 ± 12% for I10, JA and FA, respectively). For the 10-cm deep spheres, because attenuation was greater, the underestimation was even larger (77 ± 11% for I20 and I10 and 76 ± 10% for JA and FA)

Variability of Sphere-to-Background Activity Ratio. For a given image, the variability index $100 \times \sigma/r$, quantifying how variable the r value was, depending on where the user drew the background ROI, was between 2% and 23% on the I20 images, between 4% and 21% on the I10 images, between 1% and 19% on the JA images and between 2% and 19% on the FA images. The difference in variability after scatter correction was calculated for each image, and the average differences over all 45 images are given in Table 6. The variability was significantly reduced when calculating the S/B ratio from I10, JA or FA images compared to I20 images. The variability was also

TABLE 3
Median Sensitivity Values Over All Ten Observers Depending on Sphere Size and Sphere Depth

Sphere size (mm)	I20		I10		JA		FA	
	d5	d10	d5	d10	d5	d10	d5	d10
13	78%	36%	93%	36%	64%	64%	84%	45%
16	86%	83%	100%	86%	86%	83%	86%	97%
28	100%	100%	100%	100%	100%	96%	100%	96%

d5 = 5-cm-deep spheres; d10 = 10-cm-deep spheres; FA = factor analysis; I10 =10% energy window; I20 = 20% energy window; JA = Jaszczak method.

TABLE 4
Median Sensitivity Values Over All Ten Observers Depending on Heart-to-Normal (H/B) Tissue Activity Ratio

H/B activity ratio	I20	I10	JA	FA
<12	96%	98%	91%	96%
>12	61.5%	70%	71.5%	71.5%

FA = factor analysis; I10 = 10% energy window; I20 = 20% energy window; JA = Jaszczak method.

significantly lower when using JA or FA images compared to I10 images. There was no significant change in variability between JA and FA images.

DISCUSSION

Many scatter correction methods have been described in the literature, but scatter correction is still far from being widely used in clinical settings. Very few reports have described how scatter correction might affect the interpretation of clinical images (*10–16*), which may explain why scatter correction has not become part of the standard image-processing procedures. Even if the effects of scatter correction are not as dramatic as those of attenuation correction, there are certainly some indications for which scatter correction could be used with benefit, either to improve lesion detection or to make quantitation more accurate (*10,11,14–16*). Our assumption was that ^{99m}Tc-MIBI scintimammography might be one of them. Indeed, the detection of breast lesions is impeded by both attenuation and scatter. The detection of small lesions close to the chest wall or to the liver may be particularly hindered by heart and liver activities, which create a halo of scatter in the surrounding regions. To investigate whether scatter correction might be helpful in these difficult conditions, we conducted phantom experiments. Our main concern in the design of the phantom was not to closely reproduce the anatomy of the breast and neighboring structures but only to create scattering conditions close enough to those encountered when imaging breast lesions close to the chest wall. The small interior cylinder simulated heart activity, whereas the spheres fixed to this cylinder simulated lesions next to the chest wall. The activity ratios were chosen to span a wide range of imaging conditions. The tumor-to-normal tissue activity ratio seen in clinical studies has been reported to be 1.82 ± 0.95 in 20% window images (*20*) and to vary from 1.1 to 5.8 in 10% images (*1–3,21*), consistent with the values measured in our phantom experiments (varying from 1 to 5.1). The S/H activity ratios were set at 0.344, 0.526 and 1 in our phantom study. The S/H activity ratios measured in the resulting images were between 0.1 and 0.8, in agreement with the values typically observed in clinical studies. For instance, Scopinaro et al. (*22*) reported values ranging from 0.20 to 1.08. For each acquisition, the data were acquired so that at least 2 million counts were recorded in the 20% energy window. However, the list mode was processed to consider three counting statistics, corresponding to 500 kilocounts and 1 and 2 million counts in the 20% energy window, respectively. These values span the range of counts typically acquired in a scintimammogram when using conventional protocols (20/30-mCi injection and 10-min postinjection imaging) (*22,23*).

TABLE 5
Distribution of Scores Obtained by Summing All Scores Given by All Ten Observers

	I20	I10	JA	FA
Definite and accurate	386	443	447	493
Probable and accurate	279	268	261	250
Equivocal	96	78	71	65
Probable and inaccurate	77	72	83	65
Definite and inaccurate	82	59	58	47

FA = factor analysis; I10 = 10% energy window; I20 = 20% energy window; JA = Jaszczak method.

TABLE 6
Average Percentage Differences in Sphere-to-Background Activity Ratio r and Average Differences in Variability when Calculating Sphere-to-Background Activity Ratio Between Different Types of Images

Methods	Average difference in r (paired Wilcoxon test results)	Average difference in variability (paired Wilcoxon test results)
I10-I20	+1.01 ($p < 0.01$)	−1.24 ($p < 0.01$)
JA-I20	+8.96 ($p < 0.01$)	−4.13 ($p < 0.01$)
FA-I20	+7.74 ($p < 0.01$)	−3.90 ($p < 0.01$)
FA-JA	−0.71 (NS)	0.24 (NS)
FA-I10	+6.52 ($p < 0.01$)	−2.66 ($p < 0.01$)
JA-I10	+7.66 ($p < 0.01$)	−2.90 ($p < 0.01$)

FA = factor analysis; I10 = 10% energy window; I20 = 20% energy window; JA = Jaszczak method.

Scatter Corrections. Four types of images have been investigated. The 20% energy window is the method most often used for ^{99m}Tc imaging. The 10% energy window has been used in some scintimammographic studies to reduce scatter and facilitate lesion detection (*3*). The JA method is readily available on most gamma cameras, provided that acquisitions in two different energy windows can be performed simultaneously. Postprocessing is simple (subtraction of two images), and the method has been shown to yield contrast enhancement and improved quantitation compared to 20% images (*14,17,19*). The FA-based scatter correction is a more sophisticated method requiring a multiwindow acquisition device (typically 30 energy windows for ^{99m}Tc) or list mode with energy, and the dedicated factor analysis software. The method provides more accurate results than the JA method (*19*), although it remains unclear whether the price to pay in terms of hardware and software requirements is worth it.

Visual Analysis. Because scintimammographic images are mostly interpreted visually for the detection of breast lesions, we studied whether scatter correction affected the visual analysis. The image base was deliberately biased to contain only images in which the detection of the sphere was not obvious. Indeed, it is clear that scatter correction would not be of any value for improving detection performance when the detection of the sphere was already obvious on the 20% images. Therefore, the sensitivity and specificity figures obtained on this image base may not be reflective of what would be observed on the pool of images acquired in a clinical setting. Using the 20% images, the mean sensitivity over all observers (74%) was, indeed, on the lower side of the sensitivity values reported in the literature (*6*). The contents of the borderline image base (Table 1) gave some indications of what borderline real cases might be: to be difficult to detect, 28-mm^3 spheres had a low S/B activity ratio (averaging 2.1 and 3.6 at 5- and 10-cm depths, respectively). On the other hand, small spheres (13 and 16 mm) were difficult to detect at a 10-cm depth, even with a high S/B

activity ratio (averaging 13.4 and 12.3 for 13- and 16-mm^3 spheres, respectively).

For visual analysis, the display settings are particularly important. Therefore, we let each observer adjust the contrast as he/she believed would permit the most accurate reading.

On borderline images, the ROC studies showed that scatter correction was definitely useful to improve detection compared to the 20% images. The detection performance was always the poorest when using the I20 images. I10, JA and FA images gave significantly better results, and the best results were obtained using FA images. Averaged sensitivity overall observers increased by 8% using FA images compared to I20 images, and specificity also tended to be higher, although this could not be proven to be significant on this sample. Looking at more specific imaging conditions (Table 3), it was found that the 13-mm^3 spheres could generally not be detected at a 10-cm depth, although they had a 13.4 ± 5.7 S/B activity ratio on the average. At a 5-cm depth and even with a lower S/B activity ratio (4.8 ± 2.0), they became detectable (sensitivity ≥70%). Unlike the 13-mm^3 spheres, the 16-mm^3 spheres could be detected at a 10-cm depth for a high S/B activity ratio (12.3 ± 5.4 on the average). Even with an S/B activity ratio of 3.7 ± 0.9, the 16-mm^3 spheres could be detected reasonably well at a 5-cm depth (sensitivity ≥80%). The 28-mm spheres were almost always detected even at a 10-cm depth and for a low S/B activity ratio (~3). Scatter correction increased sensitivity for the 13- and 16-mm^3 spheres but did not significantly improve the detection of the 28-mm^3 spheres, which were already well detected on the I20 images.

As expected, scatter correction had a larger impact when the heart activity was high (Table 4). The sphere detection sensitivity was significantly lower for a H/B activity ratio of >12 (corresponding to measured H/B >6) than for a H/B activity ratio of <12. For H/B of <12, scatter correction did not significantly increase the detection sensitivity, while the sensitivity was increased by up to 10% for H/B >12. Indeed, for high heart activity, there was a large scatter halo around the heart, making close spheres difficult to detect. Removing part of this halo by scatter correction increased the sphere detection sensitivity.

Scatter correction not only affected the sensitivity/specificity trade-off but also impacted the degree of certainty with which the decisions were made. There were more certain and accurate judgments when using I10, JA or FA images than when 20% images were interpreted. There were almost 30% more certain and accurate judgments with FA images than with I20 images, and this was accompanied by a 40% decrease in the number of certain and inaccurate judgments. The number of equivocal judgments was also reduced when reading the I10, JA or FA images compared to the I20 images.

Quantitative Analysis. Although absolute quantitation is excluded in planar scintimammography, relative quantitation has been suggested to aid in the differentiation of benign and malignant abnormalities by means of activity ratios, e.g., between tumor and normal breast tissue (*3*). There has also been some evidence that the tumor to normal breast tissue activity ratio r could help characterize malignant tumors (*24*). Ideally, one would like to find a threshold t so that all lesions with a r value higher than t would be malignant while all lesions with a r value less than t would be benign. Quantitation in planar scintimammography is hindered mostly by attenuation and also by scatter. This could explain why the tumor to normal breast tissue activity ratio r has not been proven yet to be highly correlated with the nature of the lesion. Although attenuation definitely introduces the main bias in quantitation of r (underestimation of ~56% and ~76% for 5- and 10-cm-deep spheres, respectively), the purpose of our study was to investigate whether scatter correction could at least make the estimate of r more reliable and reproducible. Indeed, calculating r involves drawing ROIs over the tumor and over the background and is therefore subject to intra- and interobserver variabilities. In theory, scatter correction should make the background activity more uniform. As a result, the background activity estimate should be less dependent on the choice of the background ROI after scatter correction, making r less variable with the location of the background ROI than without scatter correction. Our phantom experiments confirmed that scatter correction reduced the variability by which r was estimated by up to 4%. In addition, as scatter correction mainly removed scatter counts located in the background, r was significantly higher when calculated from scatter corrected images (8% higher on JA or FA images) compared to 20% images. This implies that if a tumor-to-normal breast activity ratio threshold could be found to help classify tumors, it would certainly depend on whether images were previously corrected for scatter. Different "standard" thresholds would therefore have to be defined depending on the scatter correction involved. However, we should emphasize that, because of the large bias introduced by attenuation, which depends on the very characteristics of the tumor (especially its depth), the tumor-to-normal tissue activity ratio should be used with great caution.

Comparison of the Scatter Correction Methods. The FA-based scatter correction had the greatest impact on visual analysis and yielded results significantly better than those obtained using I10 and JA images, for both ROC and diagnosis certainty analyses. Images from I10 and JA gave very close results, which were significantly better than those observed for I20 images. Regarding quantitation, JA and FA behaved very similarly and yielded a greater decrease in variability than I10, suggesting a more effective scatter correction. Overall, the factor analysis-based scatter correction method therefore seemed to be the best choice for that particular application by improving the most both the qualitative and quantitative data analyses. However, more readily available scatter corrections, such as I10 or the JA method also provided a significant improvement compared to conventional 20% images.

Although these phantom results suggest that scatter correction could be beneficial to scintimammography, they should not be extrapolated to clinical data. This study only shows that the impact of scatter correction is certainly worth investigating on patients' scintimammographic images and that one could expect an improvement in detection performance and possibly quantitation using scatter correction. Clinical studies will now be needed to precise the role that scatter correction might play in scintimammography.

CONCLUSION

This phantom study demonstrated how scatter correction might impact planar scintimammography. Scatter correction affected favorably the visual analysis of borderline images: it significantly improved the detection performance, especially for small lesions (13- and 16-mm^3 spheres), as quantified using ROC analyses. It also increased significantly the degree of certainty with which the observers gave their judgments. From a quantitative standpoint, the value of the tumor-to-normal breast tissue activity ratio significantly increased after scatter correction. This should be considered when defining threshold values for the classification of benign and malignant tumors. In addition, scatter correction improved the reliability with which this ratio was estimated, by reducing its variability depending

on the ROI location. Among the scatter correction methods used in this study, the one based on factor analysis gave the best overall results. However, using I10 or JA images also provided a definite improvement compared to I20 images for both qualitative and quantitative image analyses. Clinical studies will now be needed to confirm that scatter correction might play a significant role in scintimammography.

ACKNOWLEDGMENTS

We are grateful to Robert Di Paola, Marie-Gabrielle Dondon, André Gavoille, Nadine Guilabert, Philippe Maksud and Mélanie Pélégrini for their contributions to this work. We also thank the reviewers for their helpful suggestions.

REFERENCES

1. Khalkhali I, Cutrone J, Mena I, et al. Technetium-99m-sestamibi scintimammography of breast lesions: clinical and pathological follow-up. *J Nucl Med* 1995;36:1784–1789.
2. Khalkhali I, Cutrone JA, Mena IG, et al. Scintimammography: the complementary role of Tc-99m sestamibi prone breast imaging for the diagnosis of breast carcinoma. *Radiology* 1995;196:421–426.
3. Taillefer R, Robidoux A, Lambert R, Turpin S, Laperrière J. Technetium-99m-sestamibi prone scintimammography to detect primary breast cancer and axillary lymph node involvement. *J Nucl Med* 1995;36:1758–1765.
4. Villanueva-Meyer J, Leonard MH, Briscoe E, et al. Mammoscintigraphy with technetium-99m-sestamibi in suspected breast cancer. *J Nucl Med* 1996;37:926–930.
5. Tiling R, Sommer H, Pechmann M, et al. Comparison of technetium-99m-sestamibi scintimammography with contrast-enhanced MRI for diagnosis of breast lesions. *J Nucl Med* 1997;38:58–62.
6. Waxman AD. The role of ^{99m}Tc methoxyisobutylisonitrile in imaging breast cancer. *Semin Nucl Med* 1997;27:40–54.
7. Palmedo H, Grünwald F, Bender H, et al. Scintimammography with technetium-99m methoxyisobutylisonitrile: comparison with mammography and magnetic resonance imaging. *Eur J Nucl Med* 1996;23:940–946.
8. Palmedo H, Schomburg A, Grünwald F, Mallmann P, Krebs D, Biersack HJ. Scintimammography with Tc-99m MIBI in suspicious breast lesions. *J Nucl Med* 1996;37:626–630.
9. Buvat I, Benali H, Todd-Pokropek A, Di Paola R. Scatter correction in scintigraphy: the state of the art. *Eur J Nucl Med* 1994;21:675–694.
10. Collier BD, Palmer DW, Knobel J, Isitman AT, Hellman RS, Zielonka JS. Gamma camera energy for Tc^{99m} bone scintigraphy: effect of asymmetry on contrast resolution. *Radiology* 1984;151:495–497.
11. Yanch JC, Irvine AT, Webb S, Flower MA. Deconvolution of emission tomographic data: A clinical evaluation. *Br J Radiol* 1988;61:221–225.
12. Floyd JL, Mann RB, Shaw A. Changes in quantitative SPECT thallium-201 results associated with the use of energy-weighted acquisition. *J Nucl Med* 1991;32:805–807.
13. Rao MG. Bone imaging with energy-weighted acquisition. *J Nucl Med* 1993;34:997–999.
14. Bonnin F, Buvat I, Benali H, Di Paola R. A comparative clinical study of scatter correction methods for scintigraphic images. *Eur J Nucl Med* 1994;21:388–393.
15. Staff RT, Gemmell HG, Sharp PF. Assessment of energy-weighted acquisition in SPECT using ROC analysis. *J Nucl Med* 1995;36:2352–2355.
16. O'Connor MK, Caiati C, Christian TF, Gibbond RJ. Effects of scatter correction on the measurement of infarct size from SPECT cardiac phantom studies. *J Nucl Med* 1995;36:2080–2086.
17. Jaszczak RJ, Floyd CE, Coleman RE. Scatter compensation techniques for SPECT. *IEEE Trans Nucl Sci* 1985;32:786–793.
18. Buvat I, Benali H, Frouin F, Bazin JP, Di Paola R. Target apex-seeking in factor analysis of medical image sequences. *Phys Med Biol* 1993;38:123–138.
19. Buvat I, Rodriguez-Villafuerte M, Todd-Pokropek A, Benali H, Di Paola R. Comparative assessment of nine scatter correction methods based on spectral analysis using Monte Carlo simulations. *J Nucl Med* 1995;36:1476–1488.
20. Maurer AH, Caroline DF, Jadali FJ, et al. Limitations of craniocaudal thallium-201 and technetium-99m-sestamibi mammoscintigraphy. *J Nucl Med* 1995;36:1696–1700.
21. Diggles L, Mena I, Khalkhali I. Technical aspects of prone dependent-breast scintimammography. *J Nucl Med Technol* 1994;22:165–170.
22. Scopinaro F, Schillaci O, Mingazzini PL, et al. Technetium-99m sestamibi: an indicator of breast cancer invasiveness. *Eur J Nucl Med* 1994;21:984–987.
23. Burak Z, Argon M, Memis A, et al. Evaluation of palpable breast masses with $99Tc^{m}$-MIBI: a comparative study with mammography and ultrasonography. *Nucl Med Commun* 1994;15:604–612.
24. Maublant J, de Latour M, Mestas D, et al. Technetium-99m-sestamibi uptake in breast tumor and associated lymph nodes. *J Nucl Med* 1996;37:922–925.

Comparison of Iodotyrosines and Methionine Uptake in a Rat Glioma Model

Karl-Josef Langen, Ralf P. Clauss, Marcus Holschbach, Heinz Mühlensiepen, Jürgen C.W. Kiwit, Karl Zilles, Heinz H. Coenen and Hans-W. Müller-Gärtner

Institutes of Medicine and Nuclear Chemistry, Research Center Jülich, Jülich; and Departments of Neurosurgery and Neuroanatomy, Heinrich-Heine-University of Düsseldorf, Düsseldorf, Germany

This study compares brain tumor imaging with 3-[^{123}I]iodo-α-methyl-L-tyrosine (IMT) and 3-[$^{123/125}$I]iodo-O-methyl-α-methyl-L-tyrosine (OMIMT) to that with [methyl-^{3}H]-L-methionine (Met) in a rat glioma model by double-tracer autoradiography. **Methods:** Cells of the glioma clone F-98 were implanted stereotactically into the right basal ganglia of 22 Fischer 344 rats. After 8 days of tumor growth, the animals simultaneously were injected with a mixture of either ^{123}I-IMT and ^{3}H-Met (n = 5), ^{123}I-OMIMT and ^{3}H-Met (n = 8) or ^{123}I-IMT and ^{125}I-OMIMT (n = 9). The animals were killed 15 min after the tracer injection and cryosections of the tumor-bearing brain area were exposed to phosphor-imaging plates both immediately and after the decay of ^{123}I. Tumor-to-brain ratios (T/B) and intratumoral distribution of the different tracers and of the cresyl violet staining of the tissue were compared. **Results:** There was a significant correlation of the T/B ratios between all tracers (IMT versus Met: $r = 0.97$, $n = 5$, $p < 0.01$; OMIMT versus Met: $r = 0.94$, $n = 8$, $p < 0.001$; OMIMT versus IMT: $r = 0.95$, $n = 9$, $p < 0.001$). Intratumoral tracer distribution was similar for all tracers and the extent of tumor labeling was identical to that of the histological tumor extent. Mean values of the T/B ratios, however, were lower for IMT (2.81 ± 0.78, $n = 14$, mean ± s.d., $p < 0.01$ compared with Met) and for OMIMT (2.03 ± 0.57, $n = 17$, $p < 0.01$ compared with Met) than for Met (3.86 ± 1.12, $n = 13$). **Conclusion:** This study confirms that tumor imaging with IMT is similar to that of Met but T/B ratios of IMT are lower. OMIMT intratumoral tracer distribution and tumor size are similar to Met and IMT, but the T/B contrast is rather low and makes this amino acid less suitable for clinical application.

Key Words: amino acids; 3-[^{123}I]iodo-α-methyl-L-tyrosine; 3-[$^{123/125}$I]iodo-O-methyl-α-methyl-L-tyrosine; [methyl-^{3}H]-L-methionine; cerebral glioma; autoradiography

J Nucl Med 1998; 39:1596–1599

Radiolabeled amino acids such as [methyl-^{11}C]-L-methionine (Met) and PET enlarge the potential of conventional radiological methods for diagnosing cerebral gliomas (*1,2*). One advantage of using amino acids appears to be visualization of the degree of intracerebral infiltration by gliomas (*3,4*). In recent years, the synthetic amino acid L-3-[^{123}I]iodo-α-methyltyrosine (IMT) has been used for brain tumor imaging, which can be used in SPECT (*5–7*).

IMT is transported into the brain and into brain tumors like other large neutral amino acids (*6,8*), and its uptake can be

Received Sep. 2, 1997; revision accepted Dec. 19, 1997.

For correspondence or reprints contact: Karl-Josef Langen, MD, Institute of Medicine, Research Center Jülich, P.O. Box 1913, 52425 Jülich, Germany.